Intercomparison of the SNPP and NOAA-20 VIIRS DNB High-Gain Stage Using Observations of Bright Stars

Truman Wilson and Xiaoxiong Xiong

***Abstract*—The Visible Infrared Imaging Radiometer Suite (VIIRS) on board the Suomi-NPP (SNPP) and NOAA-20 (N20) spacecrafts is a multi-spectral Earth-observing instrument with bands covering wavelengths from visible to long-wave infrared. Among these bands is a panchromatic day/night band (DNB) with a broad spectral response ranging from 500−900 nm, and a high dynamic range spanning over 7 orders of magnitude, allowing for observations to take place during both daytime and nighttime. The DNB operates at 3 gain levels, with low-, mid-, and high-gain stages. The high-gain stage (HGS) is capable of detecting dim city lights during Earth-view observations at night as well as bright stars through the instrument space-view port. Since SNPP and N20 are at opposite points of the same orbit, each VIIRS instrument is able to observe the same stars with the DNB in successive orbits. This will allow us to make a direct comparison of the relative calibration of each instrument using stars over a range of spectral classes. In this work, we develop methodology for accurately identifying target stars in order to make proper comparisons between the DNB HGS of each instrument. We then take observations from multiple stars in order to compute the ratio in the measured irradiance for each instrument as a function of spectral class. For K-type stars, which have the least spectral change over the DNB wavelength range, we measure a calibration bias between the SNPP and N20 DNB HGS of approximately 4%, which is stable over the duration of the N20 mission.**

***Index Terms*—VIIRS, day/night band, calibration, intercomparison**

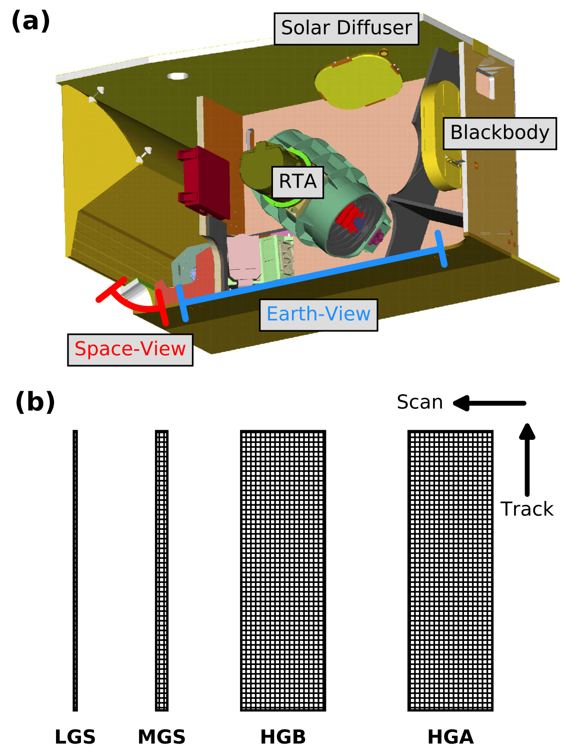

Fig. 1. (a) Cutaway diagram of the VIIRS instrument. The space-view port is an extension of the Earth-view port, viewing just beyond the Earth-limb. (b) Focal plane assembly layout for the VIIRS DNB. This example is illustrative and is not shown to scale.

I. Introduction

THE Visible Infrared Imaging Radiometer Suite (VIIRS) was launched on board the Suomi-NPP (SNPP) and NOAA-20 (N20) spacecrafts in October 2011 and November 2017, respectively. VIIRS is a whiskbroom scanning radiometer with 22 spectral bands ranging in wavelength from 0.41 to 12.2 µm [1]–[3]. These spectral bands consist of 14 reflective solar bands (RSB), 7 thermal emissive bands (TEB), and 1 panchromatic day/night band (DNB). For the RSB and TEB, there are 5 imaging bands (I-bands, 32 detectors/band) with a nadir resolution of 375 m and 16 moderate resolution bands (M-bands, 16 detectors/band) with a nadir resolution of 750 m. The VIIRS instrument also contains a set of on-board calibrators (OBC), including a solar diffuser (SD) with its associated SD stability monitor (SDSM) for calibrating the RSB, and a blackbody source (BB) for calibrating the TEB [1]. The VIIRS images are obtained using a rotating telescope assembly (RTA) which alternates scans of the Earth's surface with views of the instrument cavity where the OBC are located. During each scan, the RTA will also view deep-space through the instrument space-view (SV) port, which is an extension of the Earth-view (EV) port as seen in Figure 1(a). The SV port also provides the ability to view the Moon for an additional calibration assessment after an instrument roll maneuver is performed [4].

The VIIRS DNB constructs images using data from low-, mid-, and high-gain stages (LGS, MGS, and HGS, respectively) with the HGS further split into two stages, HGA and HGB, as seen in Figure 1(b). The HGS contains duplicate stages in order to correct for the effects of charged particle radiation, which can cause hot pixels to be present in the imagery [5]. Using these gain stages, the DNB is able to

T. Wilson is with Science Systems and Applications, Inc., Lanham, MD 20706 USA (e-mail: truman.wilson@ssaihq.com).

X. Xiong is with the Science and Exploration Directorate, NASA Goddard Space Flight Center, Greenbelt, MD 20771 USA (e-mail: xiaoxiong.xiong-1@nasa.gov).

achieve a dynamic range of over 7 orders of magnitude for the wavelength range from 500 to 900 nm. Thus, the DNB is able to observe scenes from faint city lights during nighttime observations to sunlight reflected off of clouds during daytime observations [6], [7]. In the track direction, each gain stage is composed of 672 sub-pixel detectors. In the scan direction, the LGS, MGS, and HGS have 1, 3, and 250 sub-pixel detectors, respectively. These detectors are aggregated into a set of 16 pixels in order to maintain a 750-m pixel resolution at the Earth's surface during the scan. During the EV scan, pixel aggregation of the DNB is allowed to change among 32 aggregation modes, with aggregation mode 1 near nadir with the largest angular field-of-view (FOV) and aggregation mode 32 near the edge of scan with the smallest. However, N20 has adopted a different aggregation option, Option 21 (Op21), which extends aggregation mode 21 out to the edge of scan [8]–[10]. For aggregation mode 1 (32), 66×42 (11×20) subpixels are aggregated in the scan and track directions, respectively, to form a single aggregated pixel [5].

For DNB SV observations, each scan produces an aggregated 16×16 pixel image for each gain stage in a single aggregation mode. The aggregation modes in the SV change in a 72-scan cycle, with 2 scans for each of the 32 aggregation modes (1 for each side of the half-angle mirror) with an additional 4 calibration modes (2 scans each). The additional calibration modes use extra sub-pixel aggregation for testing purposes, and are not used in the EV data [5]. Therefore, SV data from these modes will not be considered for this work. For the HGS, the DNB is sensitive enough to observe bright stars and planets through the SV port. In previous work for SNPP, stars from the Yale Bright Star Catalog (BSC) were used to monitor the on-orbit gain of the DNB HGS and to assess the relative spectral response (RSR) degradation of the SNPP VIIRS instrument [11]. Stars were also shown to be good targets for absolute calibration and spatial characterization in the PLEIADES instrument [12]. Additionally, star observations have been used for image navigation and registration as well as the monitoring of the sensor responsivity for several GOES satellite imagers [13]. For the purposes of instrument intercomparison, SNPP and N20 VIIRS are ideally suited to use stars in order to compare the relative calibration of the DNB HGS. Since SNPP and N20 are at opposite points in the same orbit, they will view the same stars in successive orbits. This close temporal proximity of observations will allow us to make a direct comparison between the two instruments with minimal impact from fluctuations in the stellar output. Also, since the comparison is relative, measurements of the absolute spectral irradiance of the target star are not needed. For the DNB MGS, the brightest stars can also be observed in the images at low signal levels. The LGS is able to see a faint images of the planet Jupiter, but is not sensitive enough to see any stars. However, with gain ratios of greater than 350 and 450 for the HGS to MGS and MGS to LGS respectively, the number of observations in these two stages is limited. Therefore, the focus of this work will be on a comparison of the two instruments using the HGS.

In this work, we present the results of a calibration intercomparison between the SNPP and N20 VIIRS DNB HGS using observations of bright stars through the SV port. The stars that we selected were from the Yale BSC (designated by the prefix HR) [14], with corresponding spectral data for the stars from the INDO-US catalog [15]. In Section II, we will show our procedure for accurately identifying stars in the image. This includes predicting the observation times, mapping the FOV of each DNB aggregation mode, and properly identifying multiple stars in a single image. Each star observation can be converted to a measured irradiance and averaged over the set of successive orbits where observing the target star is possible. In Section III, we will discuss the results of our intercomparison, which will use the ratio of SNPP to N20 star measurements. The first comparison will analyze the calibration bias between the two instruments as a function of stellar temperature, which is impacted by the change in spectral response for the SNPP DNB. Second, we will analyze the temporal stability of the calibration bias over the course of the N20 mission, which shows a stable bias of approximately 4%. Finally, in Section IV, we will present our conclusions.

II. Methodology

A. Geometry

In order to understand what observations will be possible in the VIIRS instrument configuration, we must first define our instrument geometry. This will help us to accurately identify stars in the DNB SV imagery which will be critical for making valid comparisons between the two instruments. For Earth-observing instruments, it is generally convenient to define a coordinate system relative to the instrument pointing configuration as shown in Figure 2(a). Here, the z-axis is defined as pointing towards the center of the Earth for geocentric pointing satellites, or towards normal of the ellipsoidal surface of the Earth for geodetic pointing satellites, which is the case for SNPP and N20 VIIRS [5]. The x-axis is perpendicular to z in the direction of orbital motion (track direction) and the y-axis is normal to the instrument orbital plane. For VIIRS, the instrument SV port is an extension of the EV port as shown in Figure 1(a). The SV data sector is nominally centered in the yz-plane at an angle of 24.325° from the y-axis towards the z-axis as seen in Figure 2(a). For the I- and M-bands, this data sector has an angular FOV that is approximately 1° in both the scan and track directions. For the DNB, the field of view is aggregation mode dependent, as will be shown in Section II-C.

For each orbit, the VIIRS SV port will trace out an annulus on the celestial sphere as shown in Figure 2(b). The pointing direction of the SV can be described in celestial coordinates using right ascension (α) and declination (δ). Declination is defined as the angle above or below the celestial equator (same plane as the Earth's equator) and right ascension is the azimuthal angle along the celestial equator. Since SNPP and N20 are in sun-synchronous orbits kept at a nearly fixed orbital inclination angle, the declination range of the SV FOV will be limited to approximately $\delta \in [-15°, 32°]$.This FOV will slowly shift relative to the background stars (in right ascension) as each satellite progresses in its annual orbit. As

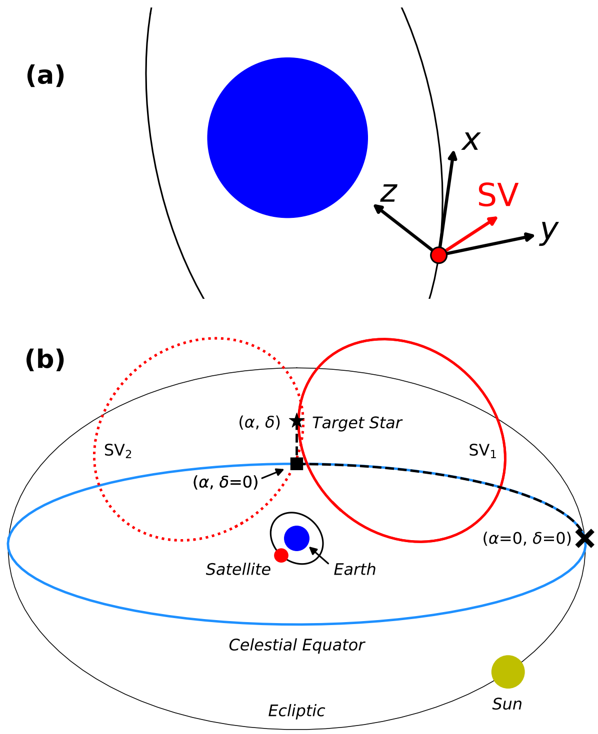

Fig. 2. (a) A diagram of the VIIRS instrument coordinate system showing the pointing direction of the SV port (red). (b) Example space-view pointing for a full orbit of the VIIRS instrument. The yellow circle represents the sun with the black line showing the ecliptic. The satellite orbit is shown around the Earth at the center of the diagram, with the blue line showing the celestial equator. A target star is shown with black dashed lines representing the derivation of the celestial coordinates (α, δ) from the celestial origin, which is located at the intersection of the ecliptic and celestial equator. The solid red trace (SV_1) shows the space-view pointing direction (see (a)) projected on the celestial sphere for a single orbit, with the dotted line (SV_2) showing the pointing in an orbit 7 weeks later.

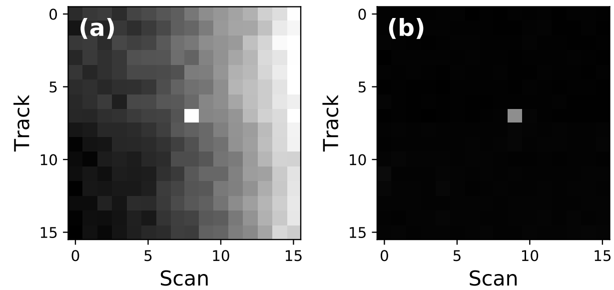

Fig. 3. A comparison of daytime and nighttime star observations for HR 996 (G-Type) from SNPP in aggregation mode 6. (a) A daytime observation showing straylight contamination across the image. (b) A night time observation showing a relatively flat background level. Both images are set to the same relative scale.

the FOV shifts, stars will enter the FOV on the leading edge of the SV annulus and can be visible for up to 10 scans per orbit. A given star will be visible for approximately 8 consecutive orbits, which we will refer to in this work as an orbital cycle. In a single orbit, the star will move through the FOV from scan-to-scan in the track direction. In subsequent orbits, the star's position in the FOV will shift in the scan direction until it is no longer visible. Depending on the location of the star, it will come into view again on the trailing edge of the SV annulus, which can be up to 7 weeks later at the center of the declination range. Observations on the leading edge of the SV annulus will typically occur during spacecraft daytime whereas the trailing edge will typically occur during spacecraft nighttime.

For daytime observations, the SV imagery in the DNB HGS can be severely impacted by a non-uniform background due to stray light [16], as seen in Figure 3. While in principle, stray light can affect imagery in both the daytime and nighttime data, our observations show that the background of the nighttime imagery is relatively flat, and the background can be successfully removed using data from the surrounding pixels in the image. For the daytime data, the stray light contamination varies greatly at different orbital geometries and is more difficult to remove. This data can have standard deviations in the trending data greater than 4 times higher than what is seen in the nighttime data. Therefore, for the comparisons in this work, we will use only nighttime imagery in order to avoid these effects. A detailed analysis of the daytime background signal and straylight correction is the subject of on-going work.

B. Calculating Observation Times

Since background observations through the VIIRS SV occur each scan, there are a great number of images that can be analyzed to determine whether a star is in the FOV. Analyzing each individual scan is computationally intensive, therefore it would be best to reduce the number of images that we need to analyze by computing the expected timing of observations for a given star. Each star's position can be considered fixed on the celestial sphere over the timescales of these satellite missions. First, we take the star's celestial coordinates and convert them into a unit vector in the time-dependent spacecraft reference frame as defined by Figure 2(a). When the star vector is within 1° of the SV, we compute the observation time as being when the star vector passes through the spacecraft yz-plane. We then create a data subset around these computed observation times in order to locate the star of interest across multiple scans.

C. Identifying Star Observations

For this work, positive identification of stars in the DNB imagery is critical. For a given image, multiple stars can be present in the FOV. Also, for stars at low apparent visual magnitude (V_m, obtained from the BSC), it would be possible to misidentify noisy or hot pixel values as stars in the image. Therefore, to positively identify the correct stars in the images, we developed the following criteria.

First, we analyze each image using Laplacian of Gaussian blob detection (Blob LoG) from Python's *scikit-image* library [17]. Example detections can be seen in Figure 4 for both SNPP and N20 VIIRS. We add a restriction that the star must be detected in both HGA and HGB within 1 pixel in order to discriminate against noise in an individual image. To further refine our star detections, we can use the observations from several bright, isolated stars in order to create a map of the DNB FOV versus the computed location of the star in

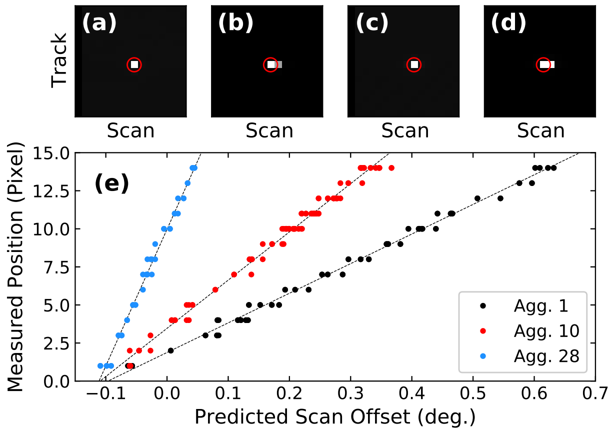

Fig. 4. Example star detection for HR 1457: (a) SNPP HGA and (b) SNPP HGB for aggregation mode 12; (c) N20 HGA and (d) N20 HGB for aggregation mode 21. The red circles indicate the star's position in the image derived from the blob detection. The NPP and N20 observations are separated by approximately 50 minutes. (e) Aggregation mode fits in the scan direction for SNPP for selected aggregation modes. Linear fits are shown as dotted black lines for each aggregation mode.

the spacecraft reference frame. Since each DNB aggregation mode has a different FOV, we will have to perform this calculation for each of the aggregation modes individually. An example of this mapping in the scan direction for SNPP aggregation modes 1, 10, and 28 is shown in Figure 4(e). We use linear fitting of the measured pixel position in the image versus the calculated angular offset of the star in the spacecraft reference frame from the SV port in both the scan and the track directions in order to characterize the pointing configuration of each aggregation mode. In the scan direction, we find that the FOV is aligned for each aggregation mode at lower pixel numbers, with the FOV of low number aggregation modes extending further at higher pixel numbers. In the track direction, each aggregation mode was found to be symmetric about the center of the image. To retrieve a predicted pixel position, we simply input our calculated angular offsets for a given image into the linear fits for a specified aggregation mode.

With this mapping in both the scan and track directions, we are able to predict the location of an arbitrary star in each image. Examples of star location predictions are shown in Figure 5 for selected stars with close neighbors. Our ability to accurately map multiple stars in a single image gives us confidence that we are identifying the correct stars in the imagery for comparison between the instruments. For this work, we also require that the location of the detected blob and our predicted position are within 1.2 pixels units in the image. For low-number aggregation modes, the FOV is relatively large, meaning that neighboring stars will appear closer together compared to high-number aggregation modes. This is shown in the example in Figure 5, (a) and (b), for aggregation modes 2 and 23, respectively. In both images, HR 1411 and HR 1412 are observed, but for aggregation mode 2, two additional stars are seen in the left part of the image due to the wider FOV. With the ability to measure the positions of neighboring stars, we also apply an additional restriction

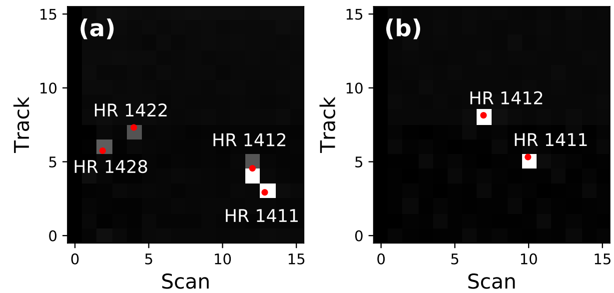

Fig. 5. Example star location predictions (red dots) for neighboring stars in SNPP for aggregation modes (a) 2 and (b) 23.

that the nearest neighboring star must be at least 2 pixel units away in the image. Therefore, for the example stars HR 1411 and HR 1412, the observation in Figure 5(a) would be rejected while the observation in Figure 5(b) would be accepted.

A list of the number of stars with observations for each instrument can be seen in Table I. In this table, we group the stars in the Yale BSC by spectral type, with a total of 9110 stars in the catalog. For SNPP, we have positive detections for 3441 stars, with the most occurring for K-type stars at 792. For N20, we detect nearly the same stars, with just 2 F-type stars lacking detection in comparison to SNPP. For some stars, only a few detections occur, and if we filter our observations by those with at least 100 night time observations, we see a larger discrepancy between the SNPP and N20 observations. This is simply due to the shorter mission duration of N20 relative to SNPP. If we look at only the brightest stars ($V_m \leq 4.0$) with at least 100 night time observations, these numbers are reduced further, to 135 and 83 for SNPP and N20, respectively.

D. Calculating the Stellar Irradiance

After, identifying the observations, we can compute the irradiance of each observation by integrating the background-subtracted signal, dn, over a 3×3 pixel region of interest around the location of the star detection. While the sensor point spread function will cause the image of the star to spread on the FPA, in most cases the stellar flux will be almost entirely contained in a single pixel due to sub-pixel aggregation. Occasionally, the star's image will spread to a neighboring pixel as shown in Figure 5(a) for HR 1412. However, the falloff in the signal level is rapid, and a 3×3 pixel region centered on the brightest pixel will be sufficient in order to capture the entire stellar flux during integration. To this integrated signal, we apply gain and solid angle (FOV) correction factors that are time and aggregation mode dependent. The on-orbit gain for the VIIRS DNB (F-factor) is provided by the VIIRS Characterization Support Team (VCST) [18]. The irradiance of each observation of a given star, L_*, can be computed by using the following equation:

$$L_* = \sum_{i,j} dn_{i,j} \cdot F \cdot c \cdot \frac{p_{sc} \cdot p_{tr}}{h^2} \quad (1)$$

where i and j represent the pixel numbers in the scan and track directions, F is the F-factor derived from SD calibrations (on-

TABLE I

A LIST OF THE NUMBER OF STARS IN EACH SPECTRAL TEMPERATURE CLASS IN THE YALE BRIGHT STAR CATALOG [14]. WE ALSO SUBSET THE CATALOG FOR STARS BRIGHTER THAN $V_m = +4.0$. FOR EACH INSTRUMENT, WE LIST THE NUMBER OF STARS WITH AT LEAST ONE POSITIVE IDENTIFICATION IN EACH SPECTRAL CLASS. WE ALSO LIST THE NUMBER OF STARS THAT HAVE AT LEAST 100 NIGHT TIME OBSERVATIONS, AND THOSE THAT ARE ALSO BRIGHTER THAN $V_m = +4.0$. WE SEE FEWER IN THE CASE OF N20 BECAUSE OF THE SHORTER MISSION DURATION.

	Stellar Temperature Class								
Inst./Cat.	**O**	**B**	**A**	**F**	**G**	**K**	**M**	**Other**	**Total**
Yale BSC	51	1758	1965	1308	1233	2236	509	50	9110
$V_m \leq +4.0$	7	139	90	60	69	125	27	1	518
SNPP VIIRS	17	568	759	573	500	792	203	29	3441
$N \geq 100$	12	380	485	342	330	516	140	10	2215
$N \geq 100$ & $V_m \leq +4.0$	4	29	26	15	20	31	10	0	135
N20 VIIRS	17	568	759	571	500	792	203	29	3439
$N \geq 100$	5	100	172	134	144	222	68	4	849
$N \geq 100$ & $V_m \leq +4.0$	4	16	13	11	14	18	7	0	83

orbit gain), and c are the calibration coefficients. While the calibration coefficients used in VIIRS are typically polynomial coefficients, for the DNB HGS, only the linear term is used. For the F-factor data, the HGS data is derived via the LGS and MGS SD data using a ratio approach. More information on the VIIRS DNB calibration from the SD data can be found in [18]. The $p_{sc} \cdot p_{tr} / h^2$ term represents the solid angle correction, with p_{sc} and p_{tr} representing the nominal pixel size on ground at nadir in the scan and track directions, respectively, and h representing the nominal altitude of the VIIRS instrument, which is 824 km. The terms F, c, and p are aggregation mode dependent, with F also changing in time on-orbit from the SD calibrations.

The values of c and F for the HGS are provided by NASA VCST as the average between HGA and HGB. For any EV radiance retrieval, the corresponding HGA and HGB pixels are averaged together in order to form a single HGS pixel, and the measurements from the individual gain stages are not sent down from the spacecraft. For the OBC and SV data sectors, we are able to retrieve the individual measurements from both HGA and HGB. In our star measurements, we observe a slight bias between the HGA and HGB dn values of approximately 0.3% and 0.8% for SNPP and N20, respectively. However, since the EV retrievals use the average of HGA and HGB, for this work, the comparisons will be made by averaging the irradiance measurements from HGA and HGB at the pixel level.

Since the aggregation modes cycle every 72 scans, it can not be guaranteed that the observations for each instrument occur in the same aggregation mode. Therefore, in this work, we will compare the measurements for each instrument by averaging all observations for a selected star in a given orbital cycle, which typically contains on the order of 50 individual (scan level) observations. An example of this data averaging can be seen in Figure 6 for HR 1084 (K-type star) for both instruments. The error bars for the cycle-averaged data in Figure 6 represent the standard deviation of the individual measurements after a 3σ outlier rejection. For this data, a spectral correction (see Section II-E) is not applied, but will be done when performing the intercomparison between the SNPP and N20 data in Section III. While we see some variation

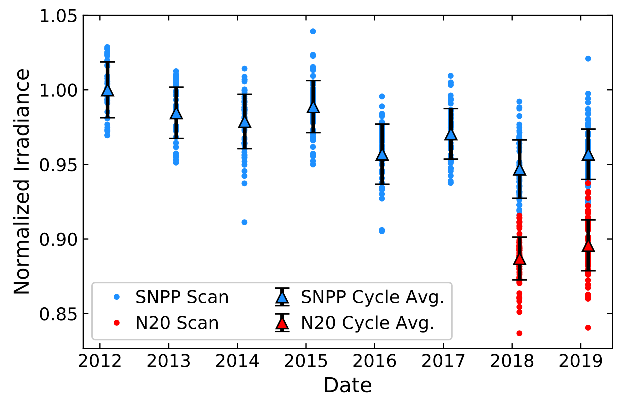

Fig. 6. Trending irradiance measurements for HR 1084 (K-type) for both SNPP (blue) and N20 (red). The dots show the individual scan measurements with the orbital cycle-averaged data overlaid with the standard deviation. The data is normalized to the first cycle-averaged data point from SNPP. No spectral correction is applied to this data.

in the measurements from year-to-year, since the SNPP and N20 measurements are made within the same orbital cycles, any variation in the stellar output should cancel out when performing the intercomparison.

E. Spectral Response Correction

In order to compare the measured results between the SNPP and N20 DNB, we need to apply a spectral response correction to the observations of each star. For SNPP, the RSR of the DNB has changed on-orbit due to contamination of the RTA mirror [19]. This change occurs rapidly early in the mission and results in the SNPP DNB being more sensitive at lower wavelengths relative to higher wavelengths later in the mission. The time-dependent (or modulated) RSR is provided by the VCST for this work. Since the launch of N20 in late 2017, the SNPP RSR has been relatively stable on-orbit. A comparison of the SNPP and N20 RSR functions can be seen in Figure 7(a).

For stars of different spectral classes, the spectral irradiance over the wavelength range of the DNB can vary significantly. Examples of the spectral irradiance for a "blue" star (HR 1427, A-type) and a "red" star (HR 1411, K-type) can be seen

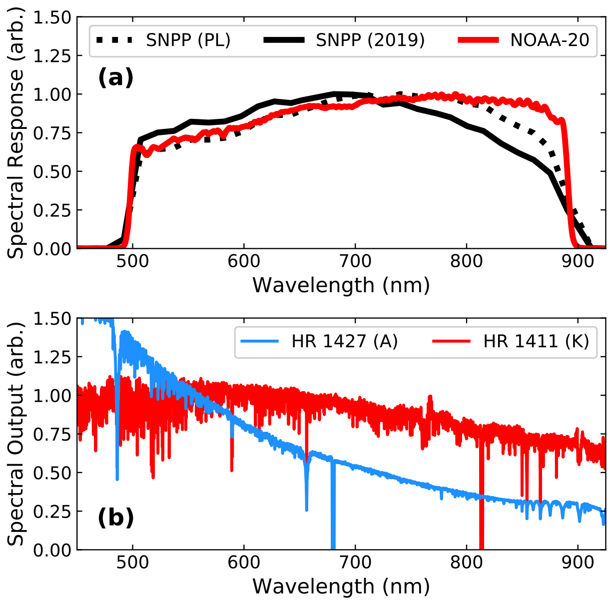

Fig. 7. (a) Relative spectral response comparison between the SNPP (pre-launch and on-orbit) and N20 DNB. (b) Example stellar spectral irradiance profiles for HR 1427 (A-type) and HR 1411 (K-type). The spectral data was obtained from the INDO-US catalog [15].

in Figure 7(b). The spectral data for the stars used in this work is from the INDO-US catalog [15], which is a database containing normalized spectral irradiances for 1273 stars. For VIIRS, there are many stars observed which are not in the INDO-US catalog. For these stars, we used the spectral data from stars with a matching spectral subclass as a substitute. When performing our comparisons in this work, a spectral response correction factor to the measured irradiance used for the intercomparison, γ_I, can be computed as follows for each instrument:

$$\gamma_I = \frac{\int \beta_I(\lambda)\, d\lambda}{\int E_*(\lambda)\, \beta_I(\lambda)\, d\lambda} \tag{2}$$

where E_* is the normalized spectral irradiance of a selected star as a function of the wavelength, λ, and β_I is the RSR of the instrument. We multiply the irradiance for each cycle-averaged irradiance measurement computed in Equation 1 by γ_I before calculating the ratio between SNPP and N20.

III. Results and Discussion

With the spectrally-corrected irradiance data for stellar observations from each instrument, we can compute the relative bias in the calibration of the two instruments by finding the ratio of each star's cycle-averaged data. By plotting this data for N20 versus SNPP, we can compute the relative calibration bias by performing a weighted linear fit to the data, as seen in Figure 8(a). For this work, we fix the intercept of the fit to pass through the origin and use the value of the calculated slope as a measure of the irradiance ratio between the two instruments. We perform this fit for data of each spectral class as seen in Figure 8(b). For this analysis, we used a spectral response correction for SNPP from both pre-launch and the

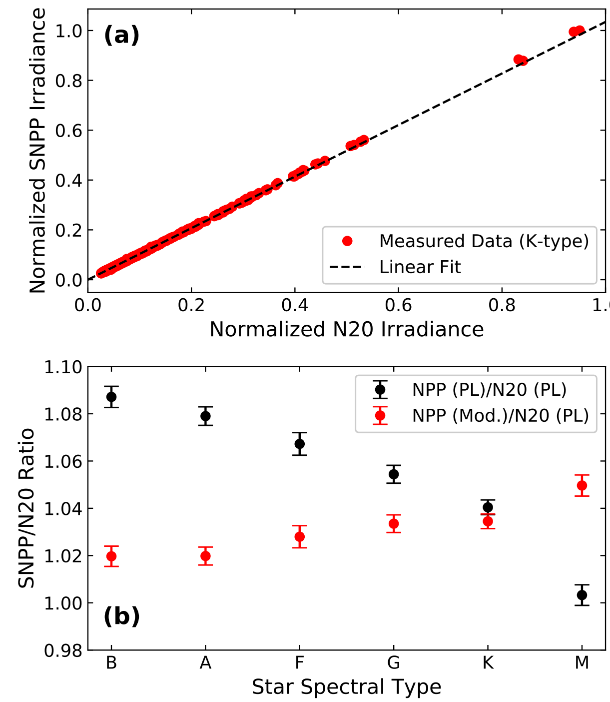

Fig. 8. Comparison of the SNPP and N20 DNB HGS ratio for different star spectral types. (a) A plot of the N20 versus the SNPP normalized irradiance. The spectral adjustment factors are applied to each axis (using the modulated-RSR for SNPP). (b) The ratio as a function of spectral type derived from the slope of linear fits like those in (a). The black data shows a spectral adjustment for SNPP using the pre-launch RSR. The red data shows a spectral adjustment for SNPP using the on-orbit modulated-RSR [19]. The error bars are propagated through the linear fits using the cycle-averaged standard deviation for each point as a weighting factor.

modulated-RSR. For N20, the pre-launch RSR is sufficient since a change in the RSR has not been detected on-orbit.

In Figure 8(b), we see that when using the pre-launch RSR, there is a large deviation in the measured ratio as a function of the stellar spectral class, with higher biases seen for higher temperature stars (more "blue"). Between B- and M-type stars, there is an 8.5% difference in the measured bias (4.5% difference between B and K). The trend versus the stellar temperature is expected, since the relative sensitivity of the NPP DNB at lower wavelengths is higher later in the mission.

If we apply the modulated-RSR for the spectral correction, we see that the bias measured as a function of the stellar spectral class is more consistent, but shows a slight trend to lower biases for higher temperature stars. In this case, the difference in the measured bias between B- and M-type stars is 3.0% (1.5% difference between B and K). A detailed study of the impact of the modulated-RSR on the SNPP DNB star measurements will be the subject of future work.

We see in Figure 8(b) that the measured bias for K-type stars is least impacted by the spectral response correction, with a change of only 0.6% between the pre-launch and modulated-RSR corrections for SNPP. This is expected because K-type stars have relatively little variation over the DNB wavelength range for both instruments (see Figure 7). The largest impacts are seen in B- and M-type stars, with 6.7% and 4.6% changes,

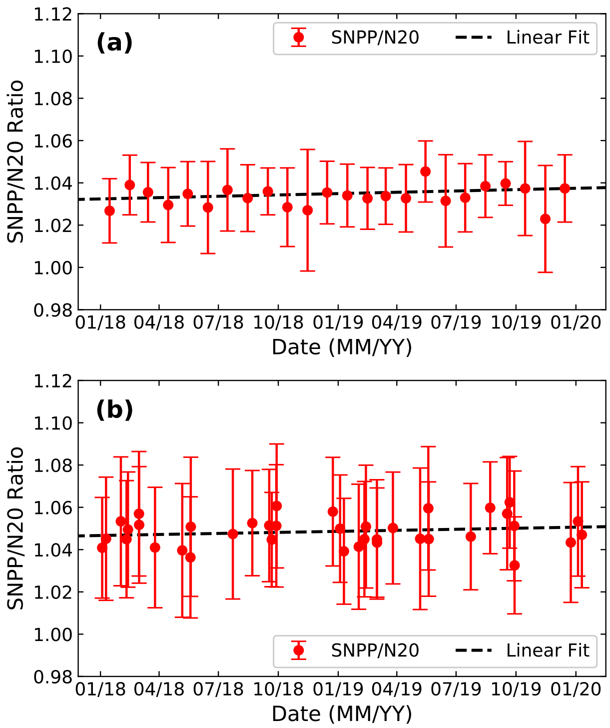

Fig. 9. Time series of the SNPP/N20 DNB HGS ratio using K-type stars. (a) All nighttime measurements are averaged for each month, and the relative bias is computed using the same method as described in Figure 8. (b) Individual cycle-averaged measurements using only stars brighter than V_m = +4.0. In both (a) and (b), the black dashed line shows a weighted linear fit to the data.

respectively. These stellar spectra show larger changes over the DNB wavelength range, particularly near the edge of the DNB RSR functions.

In addition to the relative bias as a function of stellar temperature, we can also evaluate the temporal stability in the calibration bias between SNPP and N20. For this evaluation, we will use K-type stars since they are the least impacted by the spectral response correction as shown previously. We first evaluate this using the same method that is shown in Figure 8, except now we will bin the data for each month starting in January 2018 and perform the calculation for each bin. The results for this analysis can be seen in Figure 9(a). The average bias for this monthly-averaged data is 3.6%, which matches well with the 3.5% bias calculated using all of the data shown in Figure 8(b), as expected. To the time series data, we fit a linear function weighted by the variation in each data point. This fit function shows a slight upward trend in the time series of approximately +0.26% per year, showing the relative stability of our comparison. This slight drift could be caused by relative calibration drifts or small drifts in the RSR of either instrument. However, this data alone is insufficient for making this determination and therefore will need to be investigated in the future.

The second evaluation we can do for the temporal stability comparison is to use the individual cycle-averaged measurements from only the brightest stars. In this case, we choose stars brighter than $V_m = +4.0$. The results for this comparison can be seen in Figure 9(b). For this comparison, the average bias is 4.8%, which is higher than what is measured in the monthly-averaged data. When analyzing the data at lower signal levels, we do see that a general decrease in the bias levels compared to the higher signal data. However, the individual measurements at lower signal levels have a much lower signal-to-noise ratio, but have the advantage of having far more measurements than what is available for brighter stars. This change in the measured ratio as a function of signal level may imply a slight non-linearity in the signal of one of the two instruments that is not captured when using only the linear term of the calibration coefficients in Equation 1. Such non-linearity has been observed previously in the N20 VIIRS DNB at low signal levels for aggregation modes at the edge of scan, resulting in the implementation of Op21 [8]–[10]. With absolute stellar spectral data for stars over a range of brightness levels, this effect could be investigated further in future works. For this data, we can also perform a weighted linear fit to the data, which shows a similar trend as that shown in Figure 9(a) of approximately +0.29% per year.

This bias in the ratio between the two instruments was also observed in [20] using reflected lunar light off of deep convective clouds (DCC). In this work, the authors also observed between $4-5\%$ higher radiance measured by SNPP over the DCC scenes when the lunar phase was near a full Moon, which is in good agreement with our results using the brightest K-type stars. Interestingly, this work also showed a change in the bias between the two instruments to be closer to unity when the absolute lunar phase angle increased (less reflected light from the DCC), which is also consistent with what we observed when considering stars of all brightness levels. The bias that we see from the star data in the HGS also matches well with results comparing lunar observations from SNPP to N20, with a measured difference of about 4%. This data primarily uses the LGS combined with some pixels from the MGS [21]. Since the HGS F-factor (gain) data is derived using a ratio approach from the LGS and MGS data, this work shows consistency in the calibration transfer from the LGS to the HGS from the SD data. However, an absolute calibration approach using stars for the DNB HGS is desirable for comparison, and will be the subject of future work.

IV. Conclusions

In this work, we used observations of bright stars from the Yale BSC through the SV port in order to compare the relative calibration of the SNPP and N20 VIIRS DNB HGS. We first developed methodology for the proper identification of stars in each image. By requiring our star detections to occur near the same location in both the HGA and HGB images, we can filter out noisy and hot pixels from our detections. Also, we mapped the DNB aggregation modes using observations of bright isolated stars, which allowed us to predict the location of our target stars in each image and to filter out observations where nearest neighbor stars are too close in the images. Then, for each star image, we converted the measured signal to irradiance using the gain derived from SD measurements and averaged the data over each orbital observation cycle.

We first made comparisons of the relative calibration bias as a function of stellar spectral class. We found that the on-orbit change in the SNPP RSR had a large impact on the measured bias as a function of stellar temperature, with a higher bias for hotter stars. Applying the modulated-RSR in the spectral response correction showed a significant reduction in the variation of the bias as a function of stellar temperature, but still showed a trend. In this case, we showed that the bias shows a slight increase towards cooler stars. Finally, we used K-type stars in order to assess the temporal stability of the calibration bias. Using all the data or only bright stars shows an approximately 4% greater response in SNPP compared to N20. Over the course of the N20 mission, we measure an approximately 0.3% change per year in the relative calibration.

Overall, this work shows that stars can be used as an inter-comparison source between two instruments in the same orbit, as they will be able to observe the same stars in successive orbits. With the ability to see stars over a wide spectral range, stars can also be used to evaluate the relative spectral response function of the VIIRS DNB. A full evaluation of this for SNPP will be the subject of future work. With future VIIRS missions due to launch in the coming years, the methodology developed here will be useful for evaluating the on-orbit calibration stability of the DNB in each instrument.

Acknowledgment

The authors would like to acknowledge the contributions from the VIIRS Characterization Support Team (VCST) for their valuable insights into the operations of the VIIRS instrument. In particular we would like to thank Ning Lei of VCST for providing the SNPP modulated-RSR data used for the spectral corrections in this work, and Chengbo Sun and Hongda Chen of VCST for providing the on-orbit SD F-factors for the VIIRS DNB. We would also like to thank Graziela Keller (formerly of VCST, currently at Stinger Ghaffarian Technologies/NASA JPL) for all of her valuable insights and discussions during the earliest portions of this work. Finally, we would like to thank Emily Aldoretta of SSAI for her review of this manuscript and recommendations for improvement.

References

[1] X. Xiong, J. Butler, K. Chiang, B. Efremova, J. Fulbright, N. Lei, J. McIntire, H. Oudrari, J. Sun, Z. Wang, and A. Wu, "VIIRS on-orbit calibration methodology and performance," *J. Geophys. Res. Atmos.*, vol. 119, pp. 5065–5078, 2014.

[2] C. Cao, F. Deluccia, X. Xiong, R. Wolfe, and F. Weng, "Early on-orbit performance of the Visible Infrared Imaging Radiometer Suite (VIIRS) onboard the Suomi National Polar-Orbiting Partnership (S-NPP) satellite," *IEEE Trans. Geosci. Rem. Sens.*, vol. 52, no. 2, pp. 1142–1156, 2014.

[3] X. Xiong, C. Cao, N. Lei, K. Chiang, A. Angal, Y. Li, S. Blonski, W. Wang, and T. Choi, "Early results from NOAA-20 (JPSS-1) VIIRS on-orbit calibration and characterization," *Proc. IGARSS*, vol. 2018, pp. 1112–1115, 2018.

[4] X. Xiong, J. Sun, J. Fulbright, Z. Wang, and J. Butler, "Lunar calibration and performance for S-NPP VIIRS reflective solar bands," *IEEE Trans. Geosci. Rem. Sens.*, vol. 54, no. 2, pp. 1052–1061, 2016.

[5] ATBD, VIIRS GEO, "Joint polar satellite system (JPSS) visible infrared imaging radiometer suite (VIIRS) sensor data record (SDR) geolocation algorithm theoretical basis document (ATBD)," 2013.

[6] L. B. Liao, S. Weiss, S. Mills, and B. Hauss, "Suomi NPP viirs day-night band on-orbit performance," *J. Geophys. Res. Atmos.*, vol. 118, pp. 12,705–12,718, 2013.

[7] M. Román *et. al.*, "NASA's black marble nighttime lights product suite," *Remote Sens. of Env.*, vol. 210, pp. 113–143, 2018.

[8] H. Oudrari, J. McIntire, X. Xiong, J. Butler, B. Efremova, J. Ji, , S. Lee, and T. Schwarting, "JPSS-1 VIIRS pre-launch radiometric performance," *Proc. SPIE*, vol. 9607, p. 960710, 2015.

[9] W. Wang and C. Cao, "NOAA-20 VIIRS DNB aggregation mode-change: prelaunch efforts and on-orbit verification/validation results," *IEEE J. of Sel. Topics in Appl. Earth Obs. and Rem. Sens.*, vol. 12, no. 7, pp. 2015–2023, 2019.

[10] T. Schwarting, J. McIntire, H. Oudrari, and X. Xiong, "JPSS-1/NOAA-20 VIIRS day-night band prelaunch radiometric calibration and performance," *IEEE Trans. Geosci. Rem. Sens.*, vol. 57, no. 10, pp. 7534–7546, 2019.

[11] J. Fulbright and X. Xiong, "Suomi-NPP VIIRS day/night band calibration with stars," *Proc. SPIE*, vol. 9607, p. 96071S, 2015.

[12] A. Meygret, G. Blanchet, C. Latry, A. Kelbert, and L. Gross-Colzy, "On-orbit star-based calibration and modulation transfer function measurements for pleiades high-resolution optical sensors," *IEEE Trans. Geosci. Rem. Sens.*, vol. 57, no. 8, pp. 5525–5534, 2019.

[13] I. Chang, C. Dean, D. Han, D. Crosby, M. Weinreb, J. Baucom, P. Baltimore, and X. Wu, "Improvements in the star-based monitoring of GOES imager visible channel responsivities," *Proc. SPIE*, vol. 5882, p. 58820M, 2005.

[14] D. Hoffleit and C. Jaschek, *The Bright Star Catalog, 5th rev. ed.* New Haven, CT, USA: Yale University Observatory, 1991.

[15] *INDO-US Library*. Accessed: April 26, 2019. [Online] Available: https://www.noao.edu/cflib.

[16] C. Sun, T. Schwarting, X. Geng, K. Chiang, H. Chen, and X. Xiong, "VIIRS DNB time-dependent stray light correction," *Proc. SPIE*, vol. 11127, p. 111271W, 2019.

[17] S. van der Walt, J. L. Schönberger, J. Nunez-Iglesias, F. Boulogne, J. D. Warner, N. Yager, E. Gouillart, T. Yu, and the scikit-image contributors, "scikit-image: image processing in Python," *PeerJ*, vol. 2, p. e453, 6 2014. [Online]. Available: https://doi.org/10.7717/peerj.453

[18] H. Chen, X. Xiong, C. Sun, X. Chen, and K. Chiang, "Suomi-NPP VIIRS daynight band on-orbit calibration and performance," *J. Appl. Remote Sens.*, vol. 11, no. 3, p. 036019, 2017.

[19] N. Lei, X. Xiong, and B. Guenther, "Modeling the detector radiometric gains of the Suomi NPP VIIRS reflective solar bands," *IEEE Trans. Geosci. Rem. Sens.*, vol. 53, no. 3, p. 1565, 2015.

[20] C. Cao, Y. Bai, W. Wang, and T. Choi, "Radiometric inter-consistency of VIIRS DNB on Suomi NPP and NOAA-20 from observations of reflected lunar lights over deep convective clouds," *Remote Sens.*, vol. 11, no. 8, p. 934, 2019.

[21] X. Xiong, T. Wilson, A. Angal, and J. Sun, "Using the moon and stars for VIIRS day/night band on-orbit calibration," *Proc. SPIE*, vol. 11151, p. 11151Q, 2019.

Truman Wilson received the B.S. and Ph.D degrees in Physics from Colorado State University, Fort Collins, CO, USA, in 2007 and 2013, respectively.

He is currently a Lead Research Scientist for the MODIS Characterization Support Team and the VIIRS Characterization Support Team at Science Systems and Applications, Inc., Lanham, MD, USA.

Dr. Wilson was awarded a National Research Council Postdoctoral Fellowship at the National Institute of Standards and Technology, Gaithersburg, MD, USA, in 2013.

Xiaoxiong Xiong received the B.S. degree in optical engineering from the Beijing Institute of Technology, Beijing, China, and the Ph.D. degree in Physics from the University of Maryland at College Park, College Park, MD, USA.

He is an Optical Physicist at NASA/GSFC, Greenbelt, MD, USA, currently serving as the MODIS Project Scientist and the MODIS and VIIRS Calibration Scientist. In addition to remote sensing, he had also worked in the fields of optical instrumentation, nonlinear optics, laser/atomic spectroscopy, and mass spectrometry. See http://science.gsfc.nasa.gov/sed/bio/xiaoxiong.xiong-1 for more details.

Dr. Xiong is a fellow of SPIE.